Velocity analysis of simultaneous-source data using high-resolution semblance - coping with the strong noise[a]

[a]Published in Geophysical Journal International, 204, 768-779, (2016)

Shuwei Gan, Shoudong Wang*, Yangkang Chen†, Shan Qu‡ and Shaohuan Zu**

ABSTRACT

Direct imaging of simultaneous-source (or blended) data, without the need of deblending, requires a precise subsurface velocity model. In this paper, we focus on the velocity analysis of simultaneous-source data using the NMO-based velocity picking approach. We demonstrate that it is possible to obtain a precise velocity model directly from the blended data in the common-midpoint (CMP) domain. The similarity-weighted semblance can help us obtain much better velocity spectrum with higher resolution and higher reliability compared with the traditional semblance. The similarity-weighted semblance enforces an inherent noise attenuation solely in the semblance calculation stage, thus is not sensitive to the intense interference. We use both simulated synthetic and field data examples to demonstrate the performance of the similarity-weighted semblance in obtaining reliable subsurface velocity model for direct migration of simultaneous-source data. The migrated image of blended field data using prestack kirchhoff time migration (PSKTM) approach based on the picked velocity from the similarity-weighted semblance is very close to the migrated image of unblended data.

INTRODUCTION

Simultaneous-source shooting is a breakthrough in modern seismic acquisition, which can tremendously increase the acquisition efficiency and improve the data quality (Beasley et al., 1998; Berkhout, 2008; Abma and Yan, 2009). In blended acquisition, more than one source is shot simultaneously, regardless of the interference. When more than one source is involved in acquisition, either a denser or a wider shot coverage can be obtained for a given constant acquisition period. The *wider* coverage (Figure 1b) here refers to a higher acquisition efficiency while the *denser* coverage (Figure 1a) refers to a better-sampled seismic dataset. The attractive benefits are compromised by the challenges in dealing with strong interference from simultaneous sources in the acquired seismic data. We can either separate the blended sources into individual ones as if they were acquired independently, which is also called deblending (Chen, 2014; Gan et al., 2016), or directly migrate the blended data using newly-developed imaging schemes (Verschuur and Berkhout, 2011; Tang and Biondi, 2009).

Deblending can provide similar data as the conventional acquisition and thus not require a change in post-processing and imaging algorithms, but need specific computationally expensive technique for the pre-processing (Abma and Yan, 2009; Abma, 2014). Direct imaging does not require any pre-processing steps for observed data and thus enjoys the benefit of high efficiency, but calls for a tremendously different processing workflow (Xue et al., 2014; Chen et al., 2015c).

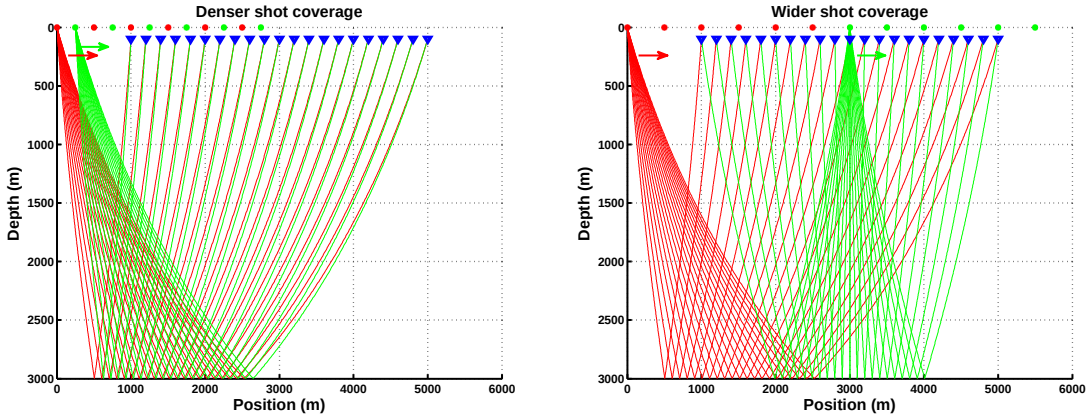

(a) (b)

Figure 1: Demonstration of the simultaneous-source geometry. (a) Two-source shooting for denser coverage. (b) Two-source shooting for wider coverage. Red points denote shot positions for source 1. Green points denote shot positions for source 2. Blue points denote receiver positions. Red and green strings denote the shooting rays. Arrows denote the shooting directions. Borrowed from Chen et al. (2014b).

Because of many reported success of deblending, more and more focus is now moved towards the direct imaging of blended data. However, one of the most important components in the direct imaging of simultaneous-source data is the macro subsurface velocity model of the targeted area. In this paper, we focus on the velocity analysis of the simultaneous-source data. We demonstrate that it is possible to directly apply the common velocity scanning procedures to the blended data in the common-midpoint (CMP) domain. We also propose to use the newly developed similarity-weighted semblance (Chen et al., 2015b; Gan et al., 2015a) to perform the velocity analysis. Both synthetic and field data examples show that the similarity-weighted semblance can help obtain higher-resolution and more reliable velocity spectrum than the conventional semblance, especially in the case of simultaneous-source data. The direct imaging of simultaneous-source data based on the directly picked velocity is also carried out via the prestack kirchhoff time migration (PSKTM) approach. The performance shows that the migrated image from blended data based on the picked velocity from similarity-weighted semblance is very close to the migrated image from unblended data.

METHOD

Blended acquisition and direct imaging

For a constant-receiver survey, the simultaneous-source data can be expressed as:

$$\mathbf{d} = \Gamma \mathbf{m}, \tag{1}$$

where $\mathbf{d}$ is the blended data, Γ is the blending operator, and $\mathbf{m}$ is the unblended data. The formulation of Γ has been introduced in Mahdad (2012) in detail. When considered in time domain, the Γ corresponds to blending different shot records onto one receiver record (node) according to the shot schedules of different shots. The Born modeling from seismic reflectivity to the primary reflections can be expressed as:

$$\mathbf{m} = \mathbf{L}\mathbf{r}, \tag{2}$$

where $\mathbf{r}$ denotes the subsurface reflectivity model and $\mathbf{L}$ denotes the Born modeling operator. One way to remove the effects caused by the blending operator Γ is first solving equation 1 and then solving equation 2, which is referred to as *deblending*. The general deblending framework can be summarized as (Chen et al., 2014a, 2015a):

$$\mathbf{m}_{n+1} = \mathbf{S}(\mathbf{m}_n + \lambda \Gamma^*(\mathbf{d} - \Gamma \mathbf{m}_n)), \tag{3}$$

where $\mathbf{S}$ is called the shaping operator, which is used to constrain the current model, and λ is the step size of the updated misfit. Γ^* denotes the adjoint of Γ. $\mathbf{m}_n$ denotes the deblended data after nth iteration.

Another way for dealing with the simultaneous-source data is to solve the following equation for $\mathbf{r}$ directly, which is known as direct imaging of blended data,

$$\mathbf{d} = \mathbf{F}\mathbf{r}, \tag{4}$$

where $\mathbf{F} = \Gamma \mathbf{L}$.

Equation 4 can be best solved using a least-squares (LS) based migration approach. More robust LS solvers involve adding constraints of structural coherency when inverting $\mathbf{r}$, either in a preconditioned LS formulation (Dai and Schuster, 2011; Chen et al., 2015c) or in a shaping-regularized LS iterative framework (Fomel, 2007b; Xue et al., 2014).

Because of the great success of deblending reported in the literature (Abma et al., 2010; Mahdad et al., 2011; Beasley et al., 2012; Li et al., 2013; Gan et al., 2015b; Zu et al., 2015; Chen, 2015) in the recent years, more and more focus is currently moving towards the direct imaging of blended data, which can be more efficient and can illuminate the surface better (Verschuur and Berkhout, 2011; Berkhout et al., 2012). It is worth mentioning that the deblending step for the massive blended data requires large computational resources (mainly for the parallel processing of a huge number of common receiver gathers) and a long processing period because of the

thousands of iterations used for each common receiver gather. If the direct imaging can obtain a good result, we can obtain a big saving in both computational resources and processing period. However, a key aspect for the success of direct imaging is the macro velocity model of subsurface. Either tomography based velocity analysis or Born-approximation wave-equation based velocity inversion, requires an initial acceptable velocity model from the very noisy blended data (Figure 9a shows an example). In the next section, we will introduce a way for obtaining high-resolution and high-fidelity velocity spectrum from blended data, using the recently developed similarity-weighted semblance.

Velocity analysis of blended data using similarity-weighted semblance

The conventional semblance is defined by Neidell and Taner (1971) as:

$$C[i] = \frac{\sum_{j=i-M}^{i+M} \left(\sum_{k=0}^{N-1} s[j,k] \right)^2}{N \sum_{j=i-M}^{i+M} \sum_{k=0}^{N-1} s^2[j,k]}, \tag{5}$$

where i and j are time sample indices, $C[i]$ denotes the conventional semblance for time index i, $2M+1$ is the length of the smoothing window along the time axis, and $s[j,k]$ is the trace amplitude at time index j and trace number k of the NMO-corrected CMP gather.

The weighted semblance introduced in Chen et al. (2015b) can be summarized as:

$$W[i] = \frac{\sum_{j=i-M}^{i+M} \left(\sum_{k=0}^{N-1} s[j,k] w[j,k] \right)^2}{\sum_{j=i-M}^{i+M} \left(\sum_{k=0}^{N-1} s^2[j,k] \sum_{k=0}^{N-1} w^2[j,k] \right)}, \tag{6}$$

where $W[i]$ denotes the weighted semblance, $w[j,k]$ denotes the weighting function for time index j and trace number k.

There have existed several weighting criteria, such as the AB semblance (Fomel, 2009), offset-prior semblance (Luo and Hale, 2012), and the similarity-weighted semblance (Chen et al., 2015b). As the similarity-weighted semblance can improve the resolution of velocity spectrum greatly, and has the possibility to subtract noise effect, we choose the local similarity (Fomel, 2007a) to weight different traces:

$$w[j,k] = \mathcal{L}(s[j,k], r[j]), \tag{7}$$

where $\mathcal{L}(\mathbf{x}, \mathbf{y})$ denotes the local similarity between traces $\mathbf{x}$ and $\mathbf{y}$, $r[j]$ denotes the jth time point for a selected reference trace $\mathbf{r}$. In this paper, the reference trace is chosen as the stacked trace using a conventional stacking technique. Figure 2 shows a demonstration of the velocity spectrum calculated using the similarity-weighted semblance compared with the velocity spectrum calculated using the traditional semblance. The left panel in Figure 2 shows a simple synthetic data with four hyperbolic events. The middle and right panels show the velocity spectrum calculated using the traditional and the proposed semblance, respectively. It is obvious that the similarity-weighted semblance is of high resolution.

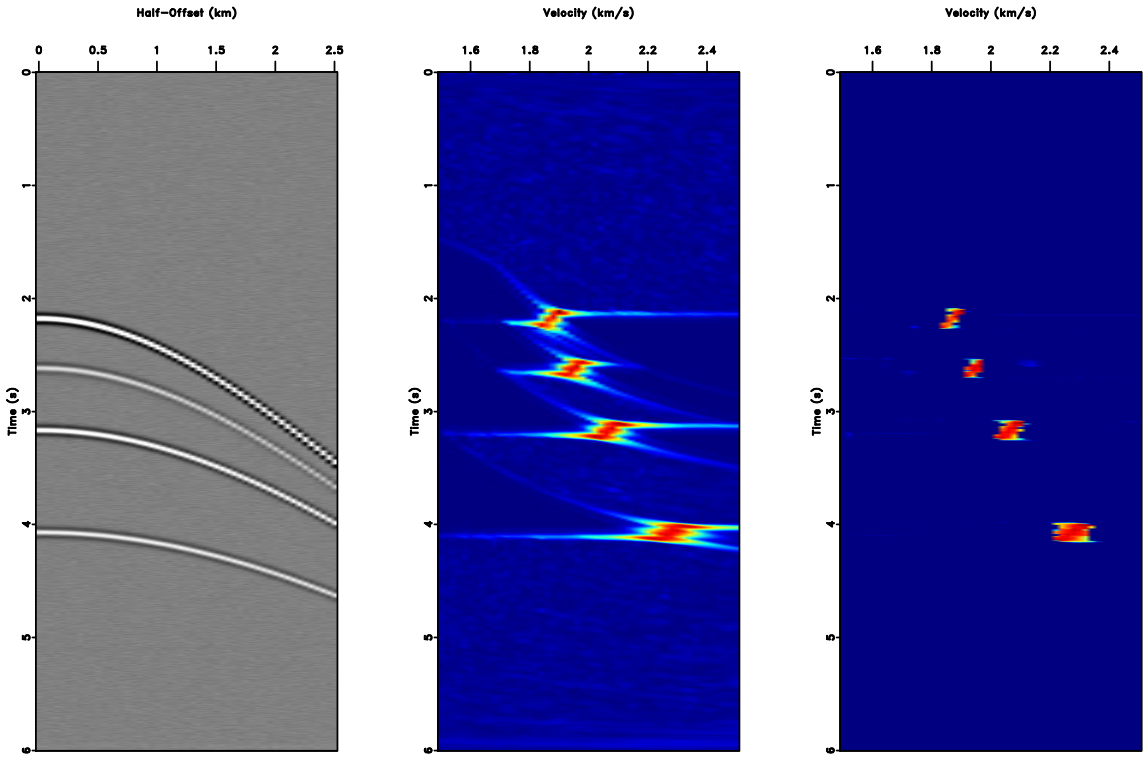

Figure 2: A brief comparison between the similarity-weighted semblance and the conventional semblance. Left: simple synthetic data. Middle: semblance map using the conventional semblance. Right: semblance map using the similarity-weighted semblance.

It is worth mentioning that, the selection of the reference trace needs several iterations in practice. It is obvious that the similarity-weighted semblance is calculated with an inherent denoising ability. The noise attenuation involved in the similarity-weighted semblance is much similar to that used in Liu et al. (2009) for attenuating random noise in the stacking process. Because of intense interference existing in the simultaneous-source data, conventional semblance will decrease the resolution because of the corruption by the blending interference. However, the beauty of the similarity-weighted semblance is that it enforces an inherent noise attenuation solely in the semblance calculation stage, without any extra process specifically designed for noise attenuation. The key element that enables the anti-noise ability of the similarity-

weighted semblance is the local similarity based weights. In the next part, we will review the basic theory of the local similarity.

Local similarity

A common way to measure the similarity between two signals is to calculate the global correlation coefficient:

$$\gamma = \frac{\sum_{i=1}^{N} a(i)b(i)}{\sqrt{\sum_{i=1}^{N} a^2(i) \sum_{i=1}^{N} b^2(i)}}, \tag{8}$$

where γ is the global correlation coefficient, N denotes the number of samples of the signals $\mathbf{a}$ and $\mathbf{b}$. In order to calculate the similarity between two signals locally, one can use the localized correlation coefficient:

$$\gamma_m(t) = \frac{\sum_{i=t-m/2}^{t+m/2} a(i)b(i)}{\sqrt{\sum_{i=t-m/2}^{t+m/2} a^2(i) \sum_{i=t-m/2}^{t+m/2} b^2(i)}}, \tag{9}$$

where $\gamma_m(t)$ denotes the local correlation coefficient, m is the local window size. Fomel (2007a) designed an elegant way to calculate the local similarity:

$$\gamma(t) = \sqrt{\gamma_1(t)\gamma_2(t)}, \tag{10}$$

$$\gamma_1(t) = \arg\min_{\gamma_1(t)} \left(\sum_t (a(t) - \gamma_1(t)b(t)) + R(\gamma_1(t)) \right), \tag{11}$$

$$\gamma_2(t) = \arg\min_{\gamma_2(t)} \left(\sum_t (b(t) - \gamma_2(t)a(t)) + R(\gamma_2(t)) \right). \tag{12}$$

Equation 10 represents that the local similarity can be expressed as the product of two vectors that are the solutions of two minimization problems. R is a regularization operator for constraining γ_1 and γ_2. R can be chosen as a local triangular smoother to enforce the smoothness of vectors γ_1 and γ_2, and then equations 11 and 12 can be solved using the shaping regularization (Fomel, 2007b):

$$\gamma_1 = [\lambda_1^2 \mathbf{I} + \mathcal{S}(\mathbf{B}^T\mathbf{B} - \lambda_1^2\mathbf{I})]^{-1}\mathcal{S}\mathbf{B}^T\mathbf{a}, \tag{13}$$

$$\gamma_2 = [\lambda_2^2 \mathbf{I} + \mathcal{S}(\mathbf{A}^T\mathbf{A} - \lambda_2^2\mathbf{I})]^{-1}\mathcal{S}\mathbf{A}^T\mathbf{b}, \tag{14}$$

where $\mathbf{A}$ is a diagonal operator composed from the elements of $\mathbf{a}$: $\mathbf{A} = diag(\mathbf{a})$ and $\mathbf{B}$ is a diagonal operator composed from the elements of $\mathbf{b}$: $\mathbf{B} = diag(\mathbf{b})$. $\mathcal{S}$ is a

smoothing operator, and λ_1 and λ_2 are two parameters controlling the physical dimensionality and enabling fast convergence when inversion is implemented iteratively. These two parameters can be chosen as the least-squares norms of $\mathbf{A}$ and $\mathbf{B}$ (Fomel, 2007a).

The local similarity algorithm can be used for the calculation of signals of any dimension. For 1D signals, the meanings of equations 13 and 14 are intuitive. For 2D or higher-dimensional signals, each signal is first reshaped into a 1D signal and then follows equations 13 and 14 to calculate the local similarity vector. The smoothing operator is applied to the 2D or multi-dimensional form of the original signal to enforce the smoothness in any dimension. Figures 3 and 4 show demonstrations for both 1D and 2D signals. Figures 3a and 3b show the same trace with different level of noise. Figure 3c shows the calculated local similarity for the 1D signal. Figures 4a and 4b show the same flattened gather with different level of noise. Figure 4c shows the calculated local similarity for the 2D signal. From the two examples, we can conclude that the local similarity can effectively obtain smooth and reasonable measurements for both 1D and 2D signals. The peaks in the calculated local similarity indicate the position of useful wavelets correctly.

EXAMPLES

The first example is a synthetic example. Figure 5 shows the unblended and blended data in the CMP domain. The blending fold is very high and thus the blended data is very noisy. It should be mentioned that before the processing, we need to apply the domain transformation. That is to say: transform the data from shot domain to midpoint domain. The domain transformation corresponds to the following transformation relation:

$$\begin{aligned} \mathbf{m} &= \frac{1}{2}(\mathbf{s}+\mathbf{r}), \\ \mathbf{h} &= \frac{1}{2}(\mathbf{s}-\mathbf{r}), \end{aligned} \tag{15}$$

where $\mathbf{m}$ and $\mathbf{h}$ denotes the midpoint and offset locations, $\mathbf{s}$ and $\mathbf{r}$ denotes the source and receiver locations. Here, we leave out the domain transformation (Chen et al., 2014b) between common shot point (CSP) domain and CMP domain, and just show the data in the CMP domain. Figure 6 shows the comparison of the velocity spectrum using conventional semblance and similarity-weighted semblance. As we know the exact velocity of this synthetic example, we can compare the velocity spectrum with the true velocity in order to judge the performance of different semblance approaches. As we can see from the comparison, the similarity-weighted semblance can obtain obviously higher resolution and more reliable spectrum. The black strings on the top of the spectrum maps denote the true velocity. The two frame boxes highlight two regions of obvious difference. From the two highlighted frame boxes, it is much clearer that the similarity-weighted semblance can get more reliable result.

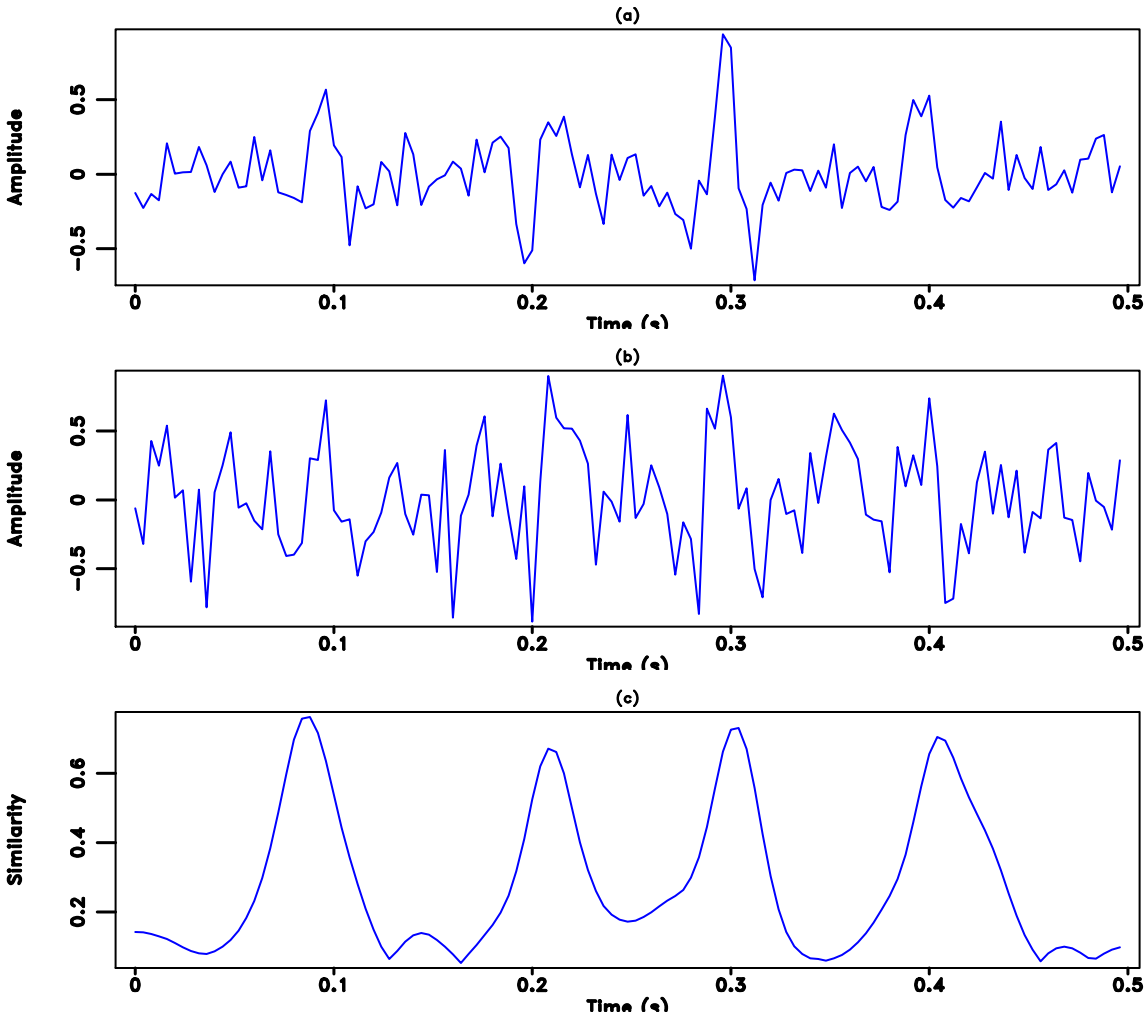

Figure 3: Local similarity for 1D signal. (a) & (b) The same trace with different level of noise. (c) Calculated local similarity.

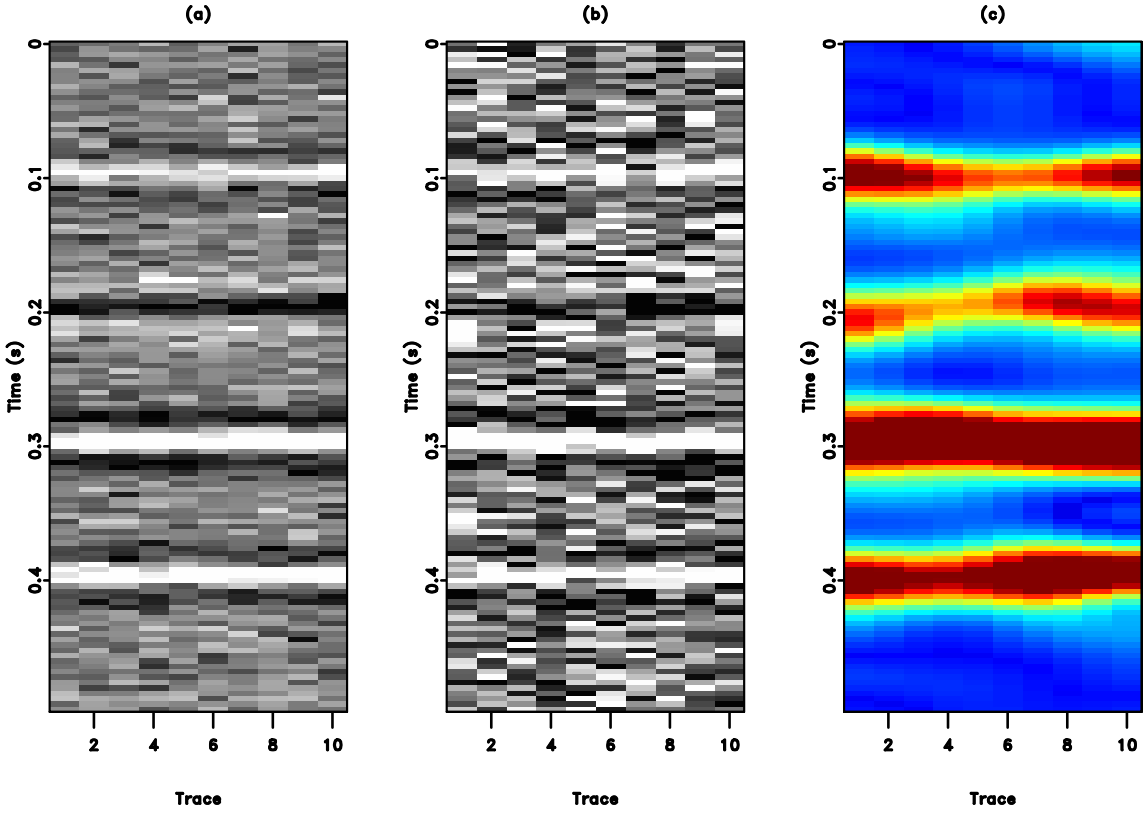

Figure 4: Local similarity for 2D signal. (a) & (b) The same flattened gather with different level of noise. (c) Calculated local similarity.

The second example is a field data example with multiples. Figure 7 shows the unblended and blended data in the CMP domain. Figure 8 shows a comparison between different velocity spectrum for both unblended and blended data. Because in this case, we do not have the true velocity model, we can only use the spectrum of unblended data as a reference. The left and middle left figures in Figure 8 correspond to the velocity spectrum of unblended data using conventional semblance and similarity-weighted semblance, respectively. The middle right and right figures in Figure 8 correspond to the velocity spectrum of blended data using conventional semblance and similarity-weighted semblance, respectively. In this case, we also have the spectrum of multiples. It is obvious that the similarity-weighted semblance can obtain higher resolution for both unblended and blended data. Comparing the middle right and right figures, we can conclude that the similarity-weighted semblance can be more reliable for velocity picking.

The third example is a numerically blended field data example in the case of high blending ratio (the interference is very strong). The numerically blended data is shown in Figure 9a. Because of the strong blended interference, it is hard to detect the useful reflections. In this example, the conventional semblance can not obtain an acceptable velocity spectrum, as shown in Figure 9b. The peaks in the velocity spectrum map are nearly smeared in the background noise. However, we can still obtain well-behaved velocity peaks, using the proposed high-resolution similarity-weighted semblance, which distinguish themselves with the background noise. The peaks can be picked either manually or automatically.

The fourth example is a numerically blended prestack field data. Figures 10a and 10b show the unblended and blended data that have been sorted from CSP gathers to CMP gathers. This example is used to simulate the independent marine-streamer simultaneous shooting (IMSSS) acquisition (Chen et al., 2014b). The blending interference is so strong that the useful reflections are nearly smeared in the noise. Figure 11a shows the velocity spectrum of the unblended data using the traditional semblance. Figure 11b shows the velocity spectrum of the blended data using the traditional semblance. Figure 11c shows the velocity spectrum of the blended data using the proposed high-resolution semblance. It is obvious that the traditional semblance can obtain good performance for clean unblended data. However, the traditional semblance cannot obtain a reasonable velocity spectrum for the blended data. Because of the strong blending interference, the traditional semblance cannot generate energy peaks in the spectrum that can be easily picked. Fortunately, the high-resolution similarity-weighted semblance can help obtain much focused peaks in the velocity spectrum that can be picked. With the automatically picked velocity (Fomel, 2009) from the velocity spectrum shown in Figure 11, we can obtain their corresponding migration results. Here, it is worth giving a brief introduction about the automatic velocity picking algorithm. Although the automatic velocity picking problem was mentioned by several researchers in the literature (Adler and Brandwood, 1999; Sarkar and Baumel, 2000; Harlan, 2001; Arnaud et al., 2004), we use the approach proposed in Fomel (2009). The main principle of the approach is to solve the following eikonal

equation

$$\left(\frac{\partial T}{\partial v}\right)^2 + \frac{1}{\alpha^2}\left(\frac{\partial T}{\partial t}\right)^2 = e^{-2w(t,v)}, \tag{16}$$

where T is the traveltime, $w(t, v)$ corresponds to the semblance spectrum, and α denotes a scaling parameter. After obtaining a finite-difference solution of equation 16, we can extract the picking trajectory $v(t)$ by tracking backward along the traveltime gradient direction.

The migrated profiles using the prestack kirchhoff time migration (PSKTM) algorithm for different cases are shown in Figure 12. Figure 12a shows the migrated profile for unblended data using the traditional semblance method. Figures 12b and 12c show the migrated profiles for blended data using the traditional semblance and the proposed high-resolution semblance, respectively. In this example, we can consider Figure 12a as the true answer, and judge the performance of different approaches by comparing the migrated results with Figure 12a. We can observe huge difference between Figures 12a and 12b. However, Figures 12a and 12c are more similar. We can confirm this observation by zooming a part from the original migrated profiles. Figure 13 shows the zoomed sections that correspond to the frame boxes shown in Figure 12. It is more obvious that Figures 13a and 13c show very similar reflections, while Figure 13b is much different from the other two cases. The erroneous reflections in Figure 13b indicate erroneous picked velocities using the traditional semblance.

CONCLUSION

We have demonstrated that it is possible to use NMO-based velocity analysis approach to obtain an acceptable velocity model from the very noisy simultaneous-source data. The similarity-weighted semblance can obtain a better velocity spectrum than the conventional semblance, with higher resolution and reliability. When the blending interference is so strong that the seismic reflections can not be observed, the similarity-weighted semblance can still show plausible energy peaks in the velocity spectrum, and the peaks can be picked easily. We use both simulated synthetic and field data examples to show the potential of the similarity-weighted semblance in velocity analysis of simultaneous-source data. We also compare the migrated images of unblended field data, and numerically blended field data using different picked velocities. The migrated image of blended data using the picked velocity from the similarity-weighted semblance is very close to the migrated image of unblended data, which shows great potential that the separation of simultaneous sources is no longer necessary.

ACKNOWLEDGEMENT

We would like to thank Pan Deng and Keling Chen for helpful discussions about similarity-weighted semblance, Jiang Yuan, Zhaoyu Jin, Ray Abma, Min Zhou, Araz

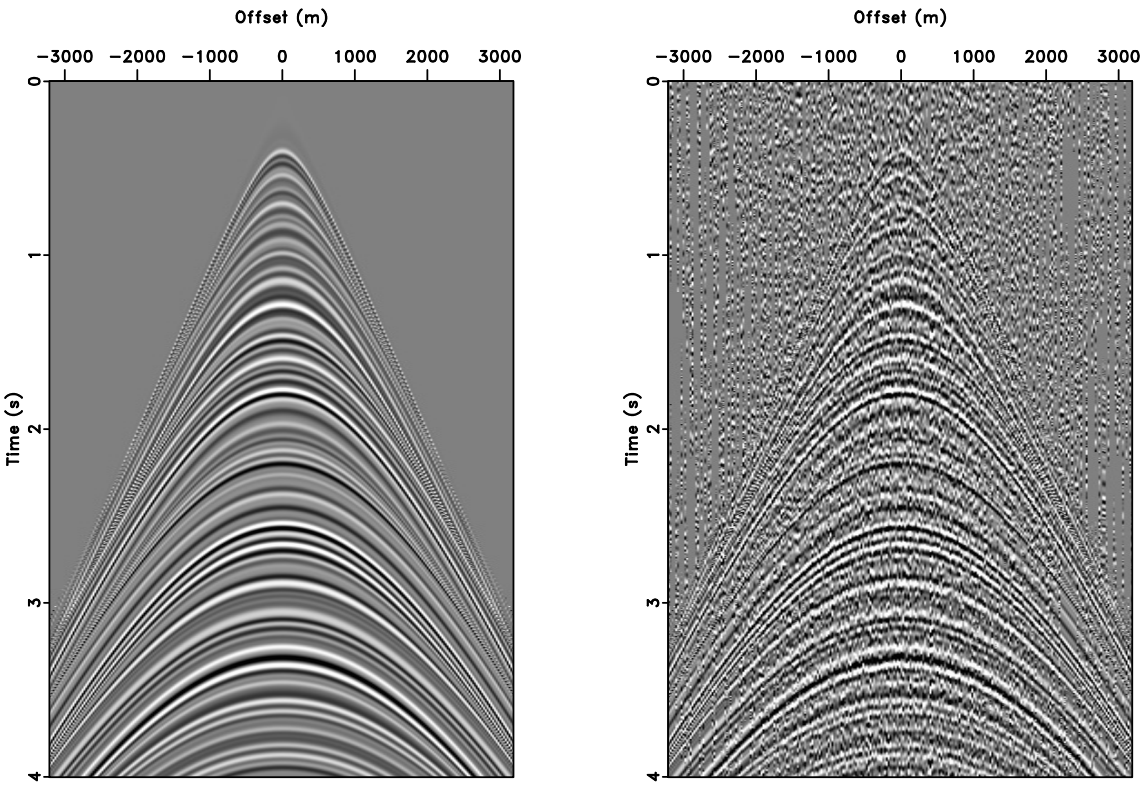

Figure 5: Synthetic data example. Left: Unblended CMP gather. Right: Blended CMP gather.

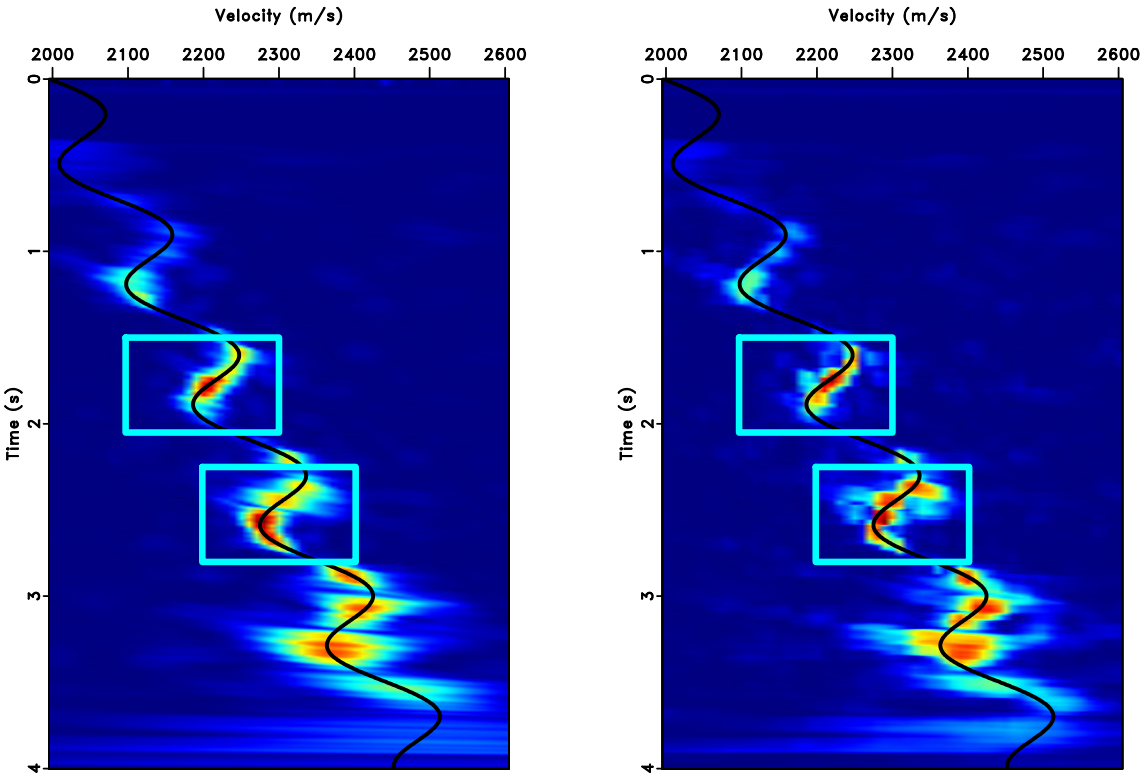

Figure 6: Left: Velocity spectrum of blended data using the conventional semblance. Right: Velocity spectrum of blended data using the high-resolution semblance.

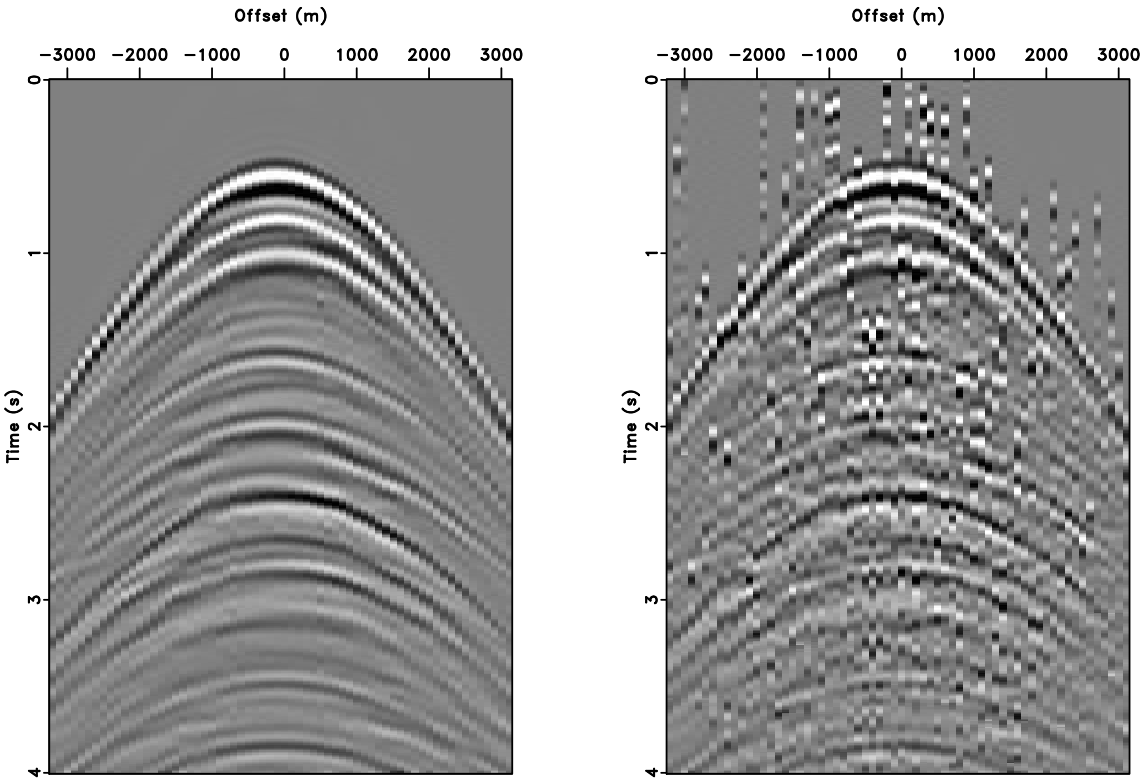

Figure 7: Field data example. Left: Unblended CMP gather. Right: Blended CMP gather.

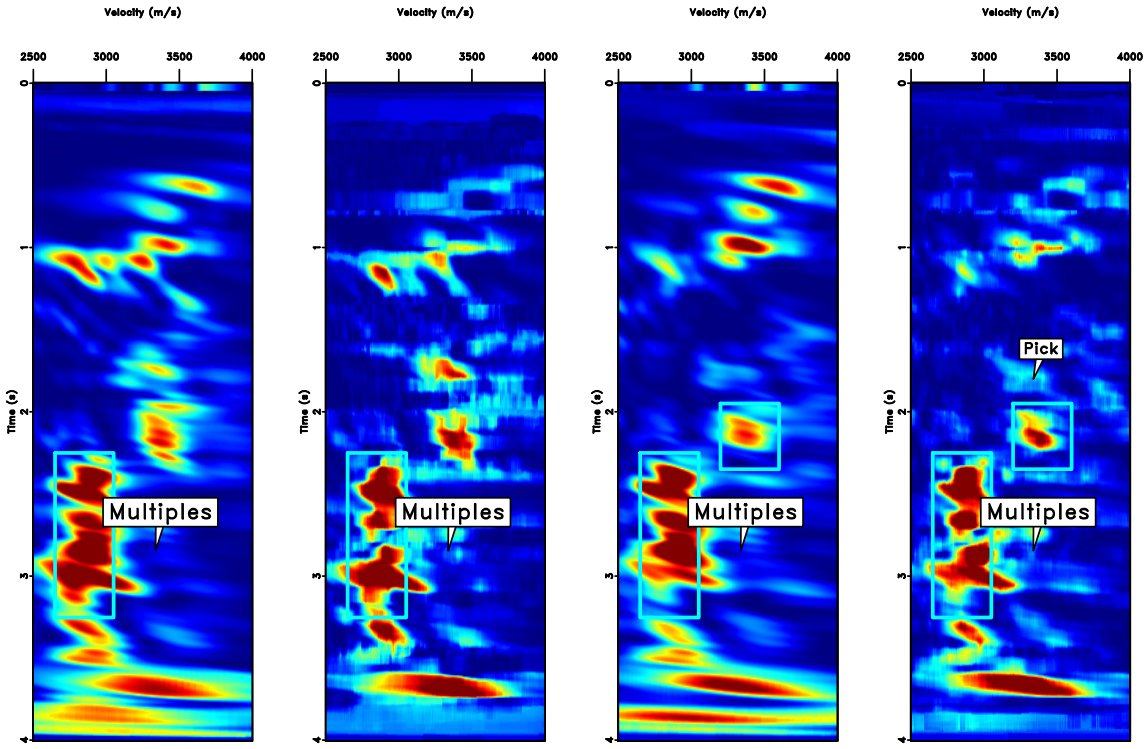

Figure 8: Left: Velocity spectrum of unblended data using conventional semblance. Middle left: Velocity spectrum of unblended data using similarity-weighted semblance. Middle right: Velocity spectrum of blended data using the conventional semblance. Right: Velocity spectrum of blended data using the high-resolution semblance.

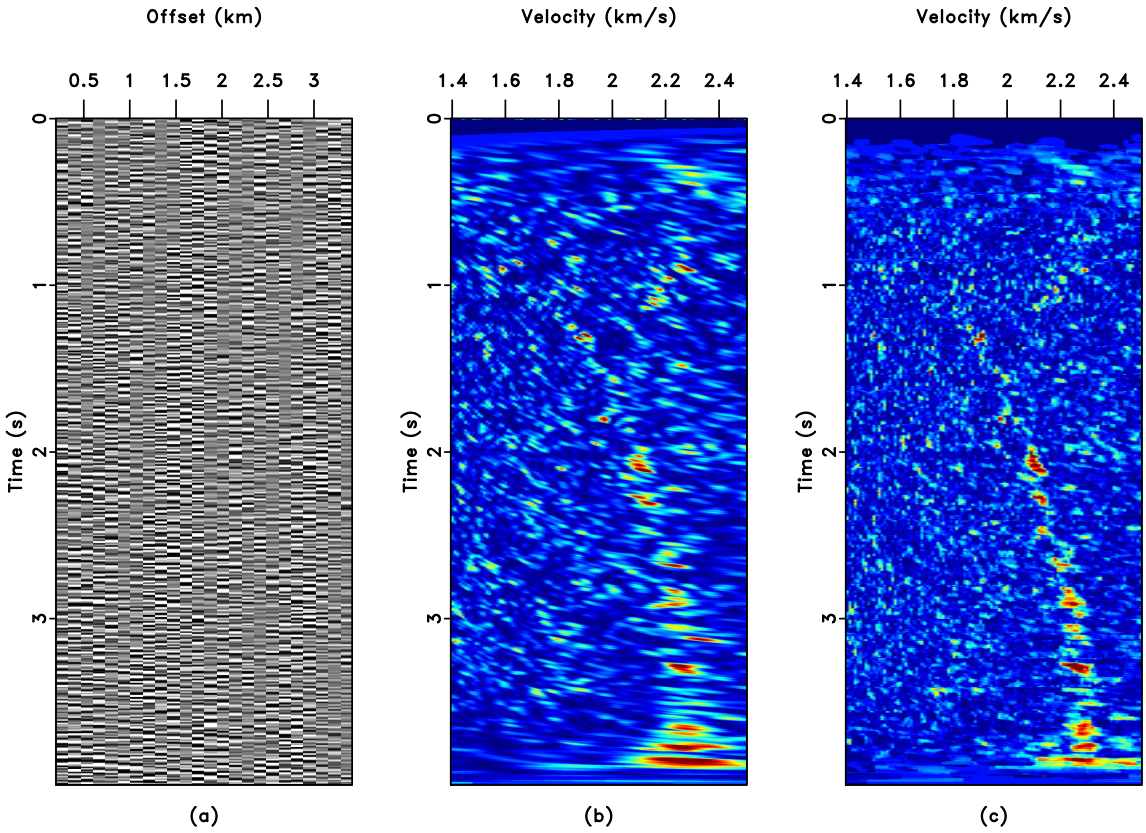

Figure 9: (a) Blended CMP gather with strong blending interference. (b) Velocity spectrum using the conventional semblance. (c) Velocity spectrum using the high-resolution semblance.

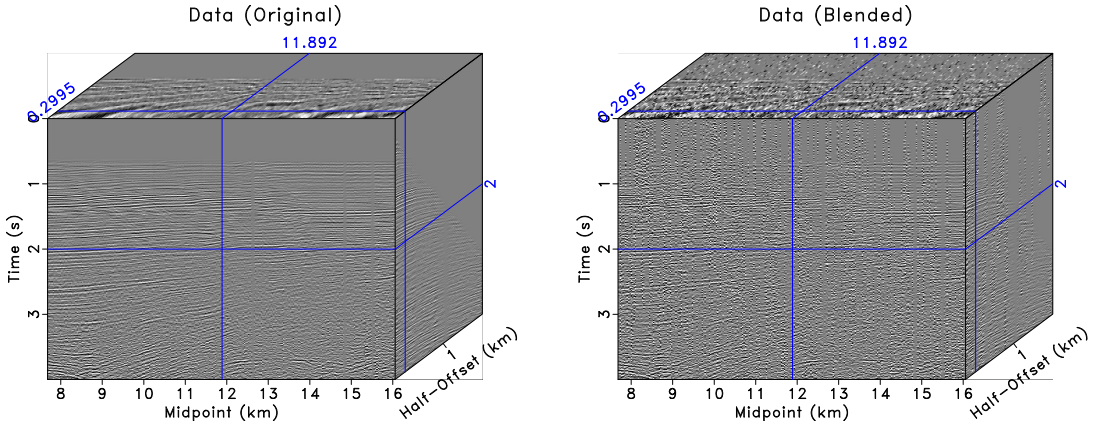

(a) (b)

Figure 10: Gulf of Mexico data example. (a) Unblended field data. (b) Numerically simulated field data.

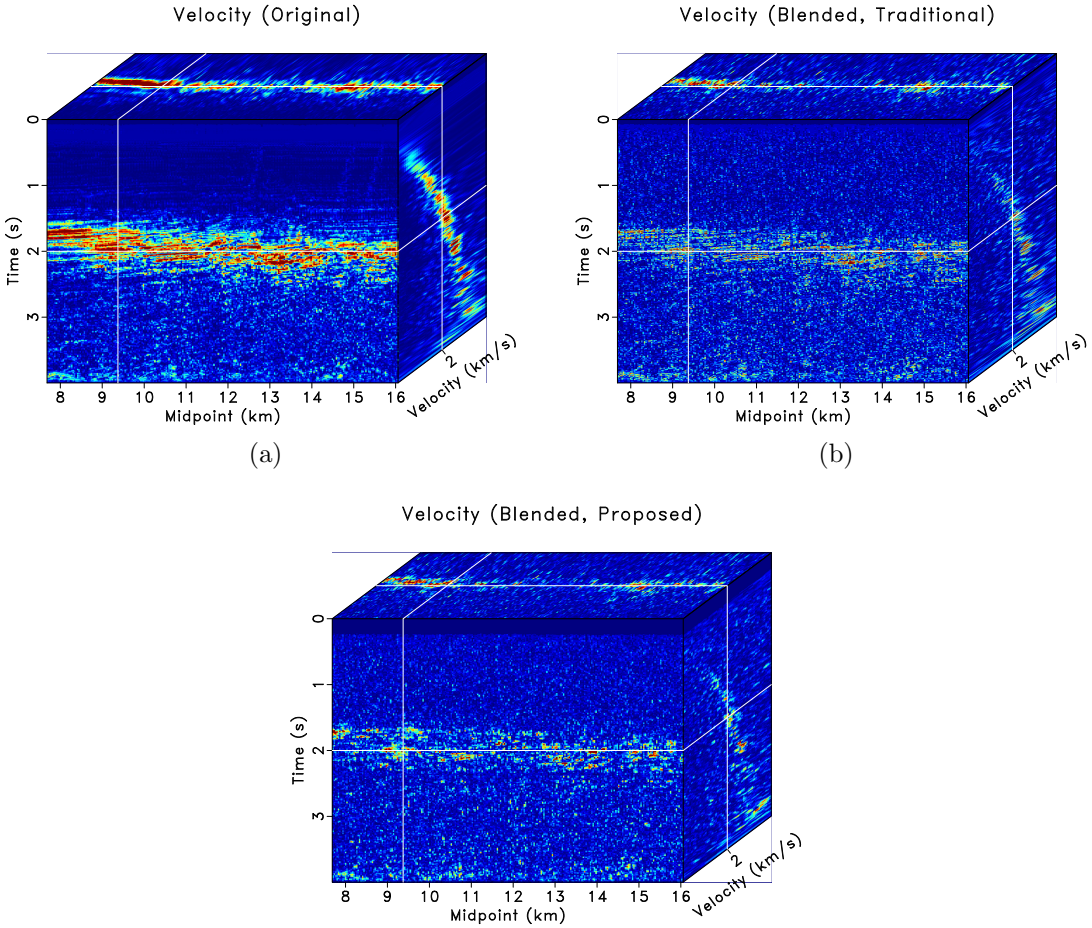

Figure 11: Comparison of velocity spectrum. (a) Velocity analysis of unblended data using the traditional approach. (b) Velocity analysis of blended data using the traditional approach. (c) Velocity analysis of blended data using the proposed approach.

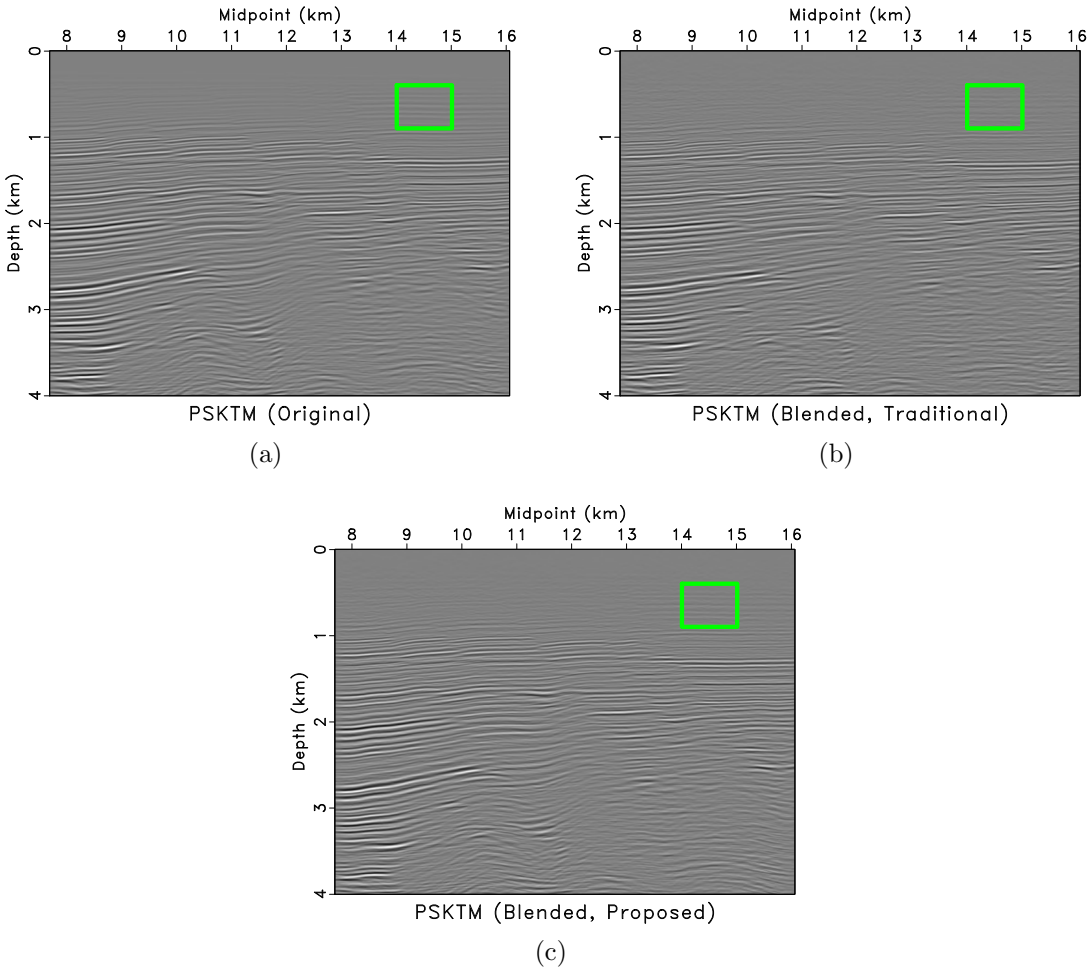

Figure 12: Comparison of migration results. (a) PSKTM of unblended data using the traditional picked velocities. (b) PSKTM of blended data using the traditional approach. (c) PSKTM of blended data using the proposed approach.

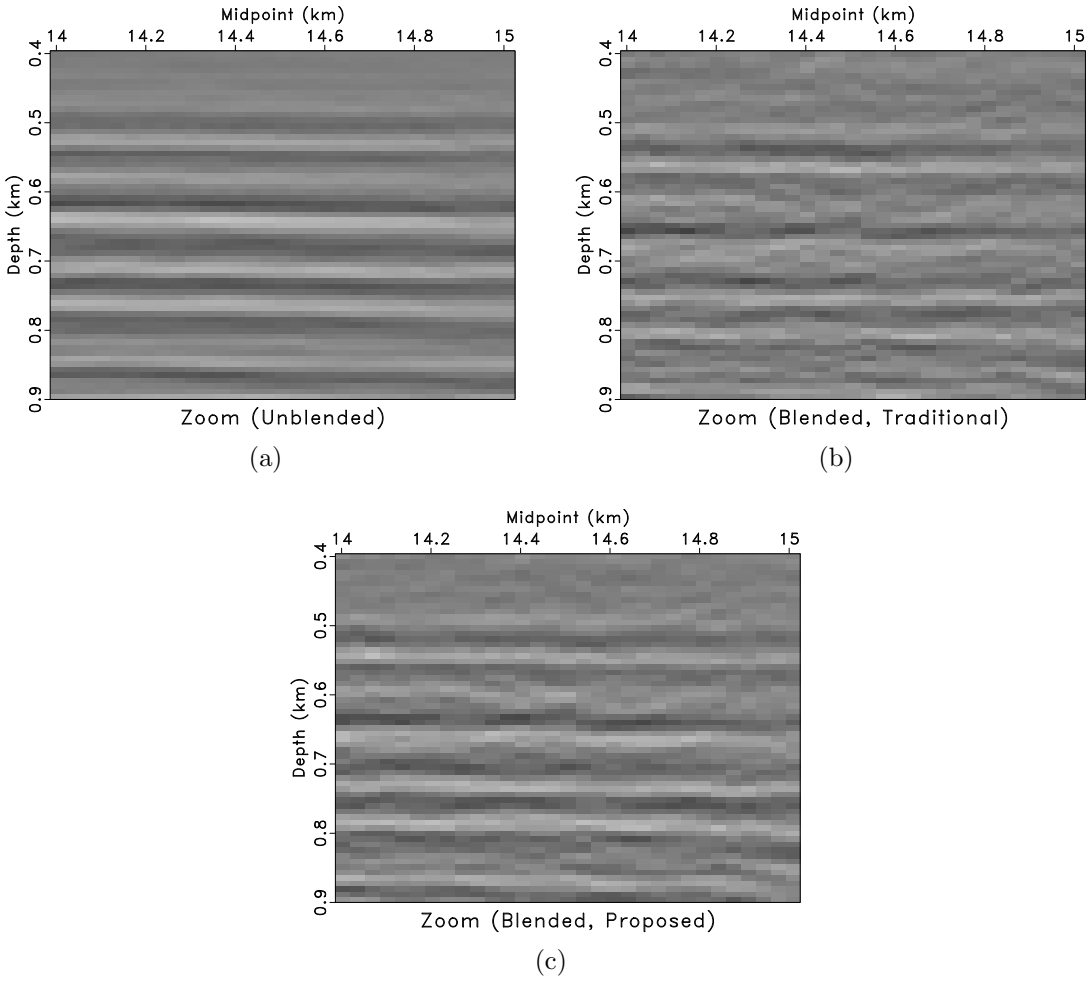

Figure 13: Comparison of zoomed migration results. (a) PSKTM of unblended data using the traditional approach. (b) PSKTM of blended data using the traditional approach. (c) PSKTM of blended data using the proposed approach.

Mahdad and Sergey Fomel for inspiring discussions about simultaneous-source acquisition. We also thank Ingo Grevemeyer, and two anonymous reviewers for constructive suggestions that improve the original manuscript greatly. This work is partially supported by the National Natural Science Foundation of China (Grant No.41274137), the National Science and Technology of Major Projects of China (Grant No. 2011ZX05019-006), National Engineering Laboratory of Offshore Oil Exploration, and the Texas Consortium for Computational Seismology (TCCS).

REFERENCES

Abma, R., 2014, Shot scheduling in simultaneous shooting: 84th Annual International Meeting, SEG, Expanded Abstracts, 94–98.

Abma, R. L., T. Manning, M. Tanis, J. Yu, and M. Foster, 2010, High quality separation of simultaneous sources by sparse inversion: 72nd Annual International Conference and Exhibition, EAGE, Extended Abstracts.

Abma, R. L., and J. Yan, 2009, Separating simultaneous sources by inversion: 71st Annual International Conference and Exhibition, EAGE, Extended Abstracts.

Adler, F., and S. Brandwood, 1999, Robust estimation of dense 3-D stacking velocities from automated picking: 69th Ann. Internat. Mtg, Soc. of Expl. Geophys., 1162–1165.

Arnaud, J., D. Rappin, J.-P. Dunand, and V. Curinier, 2004, High density picking for accurate velocity and anisotropy determination: 74th Ann. Internat. Mtg., Soc. of Expl. Geophys., 1627–1629.

Beasley, C. J., R. E. Chambers, and Z. Jiang, 1998, A new look at simultaneous sources: 68th Annual International Meeting, SEG, Expanded Abstracts, 133–135.

Beasley, C. J., B. Dragoset, and A. Salama, 2012, A 3d simultaneous source field test processed using alternating projections: a new active separation method: Geophysical Prospecting, **60**, 591–601.

Berkhout, A. J., 2008, Changing the mindset in seismic data acquisition: The Leading Edge, **27**, 924–938.

Berkhout, A. J., D. J. Verschuur, and G. Blacquière, 2012, Illumination properties and imaging promises of blended, multiple-scattering seismic data: a tutorial: Geophysical Prospecting, **60**, 713–732.

Chen, Y., 2014, Deblending using a space-varying median filter: Exploration Geophysics, doi:http://dx.doi.org/10.1071/EG14051.

———, 2015, Iterative deblending with multiple constraints based on shaping regularization: IEEE Geoscience and remote sensing letters, DOI:10.1109/LGRS.2015.2463815.

Chen, Y., S. Fomel, and J. Hu, 2014a, Iterative deblending of simultaneous-source seismic data using seislet-domain shaping regularization: Geophysics, **79**, V179–V189.

Chen, Y., Z. Jin, S. Gan, W. Yang, K. Xiang, M. Bai, and W. Huang, 2015a, Iterative deblending using shaping regularization with a combined PNMO-MF-FK coherency filter: Journal of Applied Geophysics, **122**, 18–27.

Chen, Y., T. Liu, and X. Chen, 2015b, Velocity analysis using similarity-weighted semblance: Geophysics, **80**, A75–A82.

Chen, Y., J. Yuan, Z. Jin, K. Chen, and L. Zhang, 2014b, Deblending using normal moveout and median filtering in common-midpoint gathers: Journal of Geophysics and Engineering, **11**, 045012.

Chen, Y., J. Yuan, S. Zu, S. Qu, and S. Gan, 2015c, Seismic imaging of simultaneous-source data using constrained least-squares reverse time migration: Journal of Applied Geophysics, **114**, 32–35.

Dai, W., and G. T. Schuster, 2011, Least-squares migration of multisource data with a deblurring filter: Geophysics, **76**, R135–R146.

Fomel, S., 2007a, Local seismic attributes: Geophysics, **72**, A29–A33.

———, 2007b, Shaping regularization in geophysical-estimation problems: Geophysics, **72**, R29–R36.

———, 2009, Velocity analysis using ab semblance: Geophysical Prospecting, **57**, 311.

Gan, S., Y. Chen, S. Qu, and T. Liu, 2015a, Velocity analysis of simultaneous-source data using similarity-weighted semblance: 77th Annual International Conference and Exhibition, EAGE, Extended Abstracts, DOI: 10.3997/2214–4609.201413050.

Gan, S., S. Wang, Y. Chen, and X. Chen, 2015b, Deblending of distance separated simultaneous-source data using seislet frames in the shot domain: SEG expanded abstracts: 85th Annual international meeting, 65–70.

Gan, S., S. Wang, Y. Chen, X. Chen, and K. Xiang, 2016, Separation of simultaneous sources using a structural-oriented median filter in the flattened dimension: Computers & Geosciences, **86**, 46–54.

Harlan, W. S., 2001, Constrained automatic moveout picking from semblances: http://billharlan.com/pub/papers/autopick.pdf.

Li, C., C. C. Mosher, L. C. Morley, Y. Ji, and J. D. Brewer, 2013, Joint source deblending and reconstruction for seismic data: 83rd Annual International Meeting, SEG, Expanded Abstracts, 82–87.

Liu, G., S. Fomel, L. Jin, and X. Chen, 2009, Stacking seismic data using local correlation: Geophysics, **74**, V43–V48.

Luo, S., and D. Hale, 2012, Velocity analysis using weighted semblance: Geophysics, **77**, U15–U22.

Mahdad, A., 2012, Deblending of seismic data: PhD thesis, Delft University of Technology.

Mahdad, A., P. Doulgeris, and G. Blacquiere, 2011, Separation of blended data by iterative estimation and subtraction of blending interference noise: Geophysics, **76**, Q9–Q17.

Neidell, N. S., and M. T. Taner, 1971, Semblance and other coherency measures for multichannel data: Geophysics, **36**, 482–297.

Sarkar, D., and B. Baumel, 2000, Velocity analysis in the presence of amplitude variation: 70th Ann. Internat. Mtg, Soc. of Expl. Geophys., 236–238.

Tang, Y., and B. Biondi, 2009, Least-squares migration/inversion of blended data: 79th Annual International Meeting, SEG, Expanded Abstracts, 2859–2862.

Verschuur, D. J., and A. J. Berkhout, 2011, Seismic migration of blended shot records with surface-related multiple scattering: Geophysics, **76**, A7A13.

Xue, Z., Y. Chen, S. Fomel, and J. Sun, 2014, Imaging incomplete data and simultaneous-source data using least-squares reverse-time migration with shaping regularization: 84th Annual International Meeting, SEG, Expanded Abstracts, 3991–3996.

Zu, S., H. Zhou, Y. Chen, Y. Liu, and S. Qu, 2015, A periodically variational dithering code for improving deblending: SEG expanded abstracts: 85th Annual international meeting, 38–42.